



OPEN

SUBJECT AREAS:

LASER MATERIAL
PROCESSING

SOLID-STATE LASERS

INTEGRATED OPTICS

Monolithic crystalline cladding microstructures for efficient light guiding and beam manipulation in passive and active regimes

Received
10 June 2014Accepted
23 July 2014Published
7 August 2014Yuechen Jia¹, Chen Cheng¹, Javier R. Vázquez de Aldana², Gabriel R. Castillo², Blanca del Rosal Rabes³, Yang Tan¹, Daniel Jaque³ & Feng Chen¹

¹School of Physics, State Key Laboratory of Crystal Materials, and Key Laboratory of Particle Physics and Particle Irradiation (Ministry of Education), Shandong University, 250100 Jinan, Shandong, China, ²Laser Microprocessing Group, Universidad de Salamanca, 37008 Salamanca, Spain, ³Fluorescence Imaging Group, Departamento de Física de Materiales, Facultad de Ciencias, Universidad Autónoma de Madrid, 28049 Madrid, Spain.

Correspondence and requests for materials should be addressed to F.C. (drfchen@sdu.edu.cn)

Miniature laser sources with on-demand beam features are desirable devices for a broad range of photonic applications. Lasing based on direct-pump of miniaturized waveguiding active structures offers a low-cost but intriguing solution for compact light-emitting devices. In this work, we demonstrate a novel family of three dimensional (3D) photonic microstructures monolithically integrated in a Nd:YAG laser crystal wafer. They are produced by the femtosecond laser writing, capable of simultaneous light waveguiding and beam manipulation. In these guiding systems, tailoring of laser modes by both passive/active beam splitting and ring-shaped transformation are achieved by an appropriate design of refractive index patterns. Integration of graphene thin-layer as saturable absorber in the 3D laser structures allows for efficient passive Q-switching of tailored laser radiations which may enable miniature waveguiding lasers for broader applications. Our results pave a way to construct complex integrated passive and active laser circuits in dielectric crystals by using femtosecond laser written monolithic photonic chips.

Miniature photonic devices, such as beam splitters, directional couplers, and mirroring modulators, have received a broad range of applications, including but not limited to optical telecommunications, quantum computing, biophotonic sensing, and information processing¹⁻⁷. These devices are constructed based on the optical waveguide technology. Versatile guiding structures with diverse geometries have become basic components of modern integrated photonic circuits. Compact, integratable lasers with excellent performance are particularly desirable as light sources for intricate photonic chips so as to reduce the scale of the devices⁸. Waveguide lasers have been realized in large numbers of active waveguide systems, covering broad spectral region ranging from visible to mid-infrared, with continuous-wave (CW) and pulsed regimes (Q-switched or mode-locked)⁹⁻¹³. Some excellent performances of obtained waveguide lasers have shown the potential as light sources for the development of highly integrated photonic circuits. Nevertheless, the light-beam profiles of the waveguide lasers cannot be manipulated in a flexible manner. And in most cases, researchers manufacture waveguide lasers in straight channels or planar layers that strongly limit the actual control of the spatial properties of the generated laser radiations⁸. In practice, versatile requirements on the laser beams are desired, in addition to the easily achievable single Gaussian-like profiles.

Femtosecond laser pulses with high intensities induce extremely localized modifications of material matrix through strong-field ionization processes. The femtosecond laser writing has become a powerful, widely applicable technique to implement one-step 3D micro-engineering of materials for a great variety of applications¹⁴⁻¹⁶, owing to many advantages, such as wide applicability of materials, negligible thermal-diffusion effect, and ability for maskless 3D processing¹⁵. Since the pioneering work of Davis et al. in 1996, in which optical waveguides were fabricated in a few glasses¹⁷, many research groups have utilized the femtosecond-laser writing to manufacture guiding devices in transparent optical materials, including glasses, dielectric crystals, ceramics, and organic materials, and realized applications in diverse disciplines¹⁸⁻²². Unlike the modification of glasses, in which the femtosecond laser pulses usually induce positive changes of the refractive index ($\Delta n > 0$), negative index changes

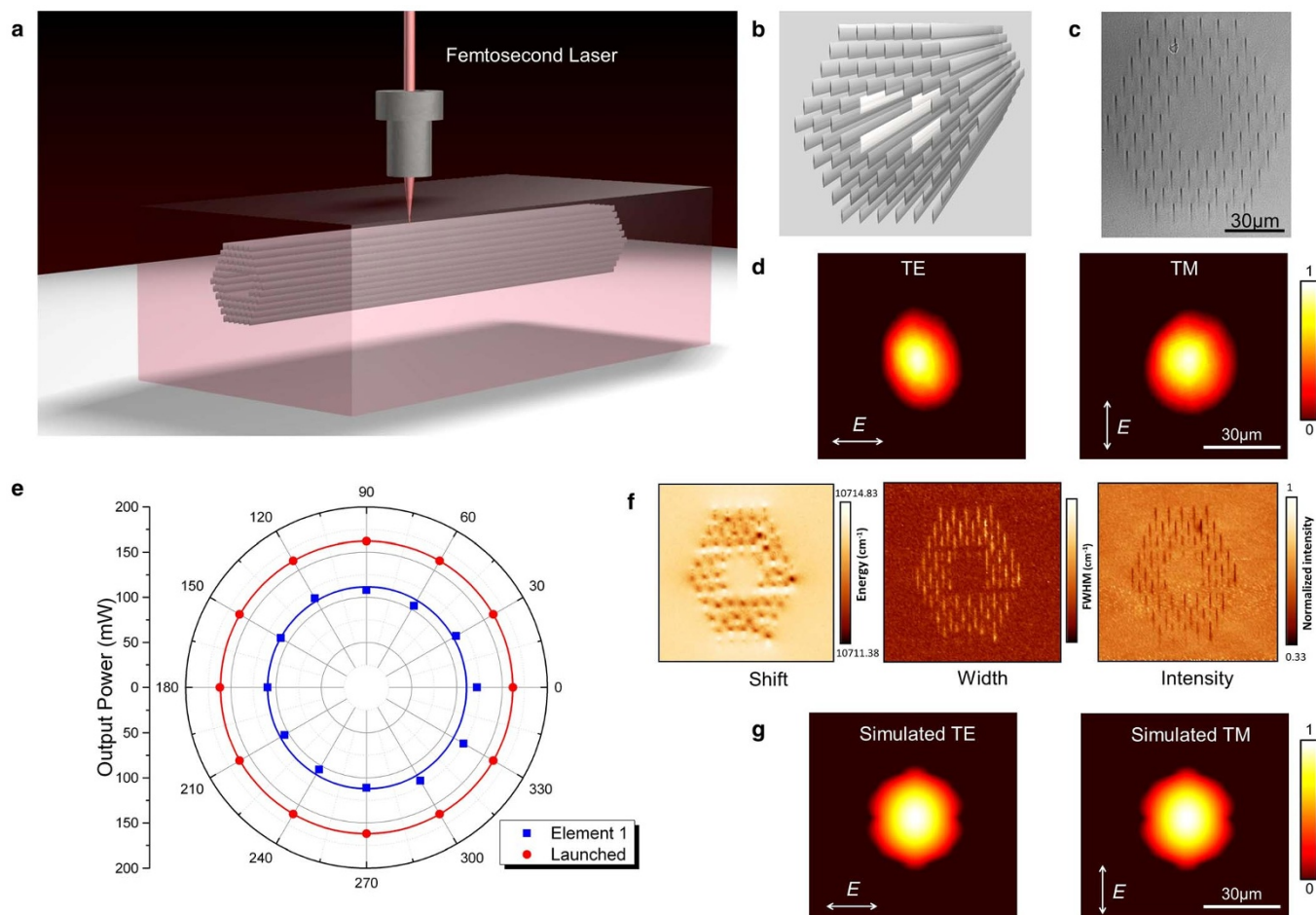


Figure 1 | Photonic structure characterization. (a), The fabrication schematic plots of a typical photonic microstructure with a guiding core surrounded by a hexagonal track array. (b), Cross-sectional sketch of the photonic microstructure. (c), Microscopic image of the cross section of the fs laser written photonic Element-1 in Nd:YAG crystal. (d), Measured near-field modal profiles along both TE and TM polarizations at 1064 nm. (e), All-angle light transmission along the transverse plane at 1064 nm. (f), Micro-photoluminescence (μ PL) mappings (spatial distributions of emitted intensity, spectral shift, and linewidth) of the photonic structure. (g), Simulated modal profiles of the guiding microstructure along both TE and TM polarizations.

($\Delta n < 0$) are typically induced in crystalline media through the femtosecond laser modifications. This, to some extent, blocks the applicability of 3D micromachining of waveguides in dielectric crystals by using femtosecond laser writing. People have produced waveguides with Type I (direct-write waveguides, guiding core located in the femtosecond-laser-written tracks of $\Delta n > 0$), Type II (stress-induced ones, guiding core typically located in the center region of two parallel tracks of $\Delta n < 0$), and Type III (depressed cladding structures, core located in the region surrounded by a number of tracks of $\Delta n < 0$) configurations in crystals¹⁹. Particularly, femtosecond laser writing has been employed to successfully implement curved waveguiding structures and waveguide lasers in Yb:YAG crystals recently, which paves a way to realize lasing in non-straight channels²³. In this work, we present a novel family of photonic structures consisting of hexagonal lattices of tracks ($\Delta n < 0$) with induced defects capable of efficient light confinement in a wide spectral range. By changing the transverse profile of the waveguide (i.e., introducing new axial defects in the appropriate positions of the lattice), the light beam manipulation of 1×2 beam splitting and ring-shaped transformation are achieved. We demonstrate here that the flexibility and convenience of femtosecond laser micro-modification enable the integration of diverse elements in a single crystal wafer, providing the possibility of simultaneous generation and manipulation of guided light beams. By using direct-pump of the monolithic integrated structures, waveguide lasing has been obtained in both CW and pulsed (passively Q-switched by graphene) regimes.

Results

The structures are fabricated in the well-known Nd:YAG (neodymium doped yttrium aluminum garnet) laser crystal, which has a cubic lattice geometry for laser oscillations at 1.06 μm . The femtosecond-laser pulses create micro-modifications in the irradiated areas of the crystal, which can be controlled by the parameters such as pulse energy, scanning speed, beam intensity distribution, and beam polarization. Figure 1a and 1b show the schematic plots of a typical photonic microstructure (with a guiding core surrounded by a hexagonally arrayed track lattice, hereafter referred to Element 1) and its cross-sectional topography, respectively. The laser inscribed tracks have a transverse length of 10 μm , and the separation between two adjacent tracks is set to 10 μm . The central core is approximately a region with area of $30 \times 30 \mu\text{m}^2$ to maintain a nearly symmetric geometry. Figure 1c depicts the optical microscope image of the cross section of Element 1 fabricated inside a 10-mm long Nd:YAG crystal. The guidance of the element is experimentally investigated by end-face coupling arrangement at wavelength of 1064 nm with a linearly-polarized CW laser. As shown in Fig. 1d for the measured near-field modal profiles, the structure supports well-confined modes along both TE and TM polarizations. This feature is similar to the depressed-cladding waveguides in Nd:YAG²⁴ produced by the femtosecond-laser writing but significantly different from the Type II structures which only guide TM modes²⁵. As to obtain thorough information of the polarization effects of the guidance, we measure the all-angle light transmission along the transverse plane (Fig. 1e). It

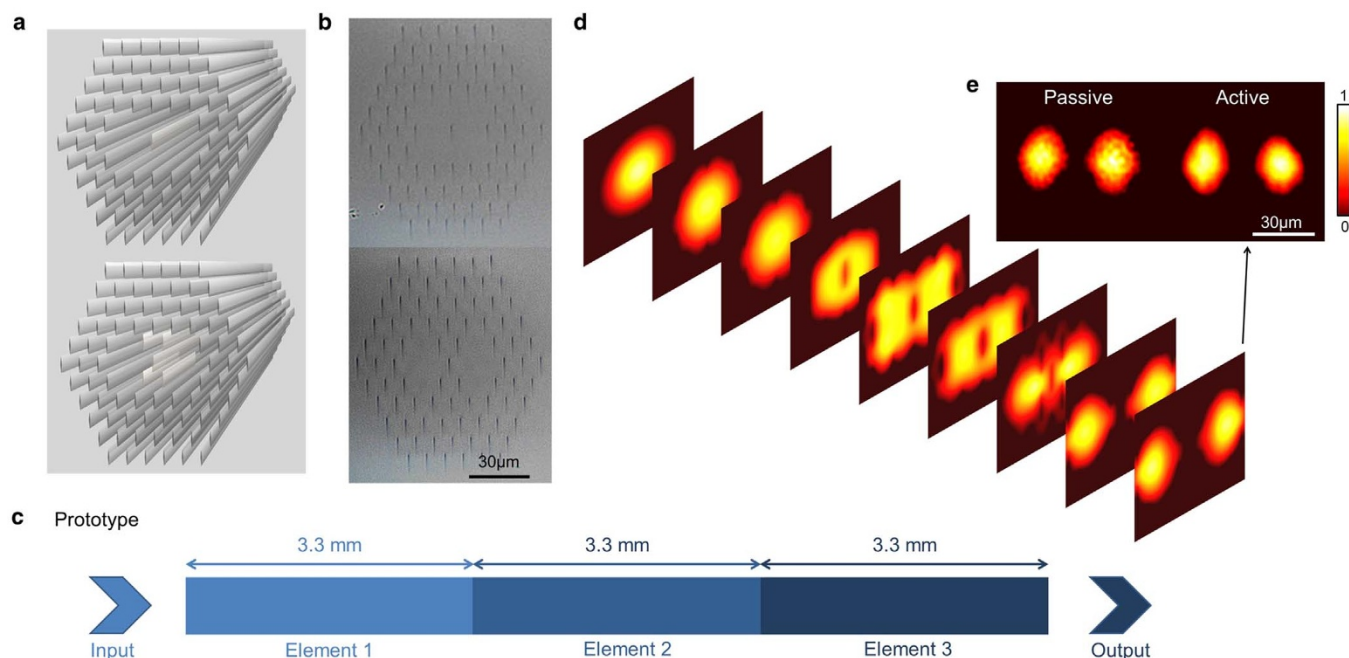


Figure 2 | Photonic structure characterization for beam splitting in passive regime. (a), Schematic images of Element 2 (top) and 3 (below). (b), Microscopic pictures of Element 2 (top) and 3 (bottom). (c), The prototype of the beam splitter with connection of Element 1, 2 and 3, with each element 3.3-mm long. (d), Simulated beam profile evolution as the 1064-nm light propagates along the photonic structure. (e), Measured intensity distributions of the beam splitter in both passive and active regimes at 1064 nm.

is found that the guidance is polarization-independent (i.e., the guidance exists for the input light at any transverse polarizations), revealing a perfect isotropic light confinement capability, which is even better than the normal Type III Nd:YAG cladding waveguides. It should be also noted that the transmitted light through the guiding structure preserves the original polarization. Finally, the propagation loss of Element 1 is determined to be ~ 0.7 dB/cm, showing an excellent light transmission property. This value is comparable with the Type II Nd:YAG dual-line waveguides (0.6–1.6 dB/cm)²⁵, and may be further reduced by increasing the guiding core volume²⁶. In addition, the amount of the track lattice layers is an important factor for light field restriction: multiple-layer track lattice offers better light confinement than single-layer structure (see Supplementary Fig. 1).

Figure 1f shows the confocal micro-photoluminescence (μ -PL) maps (spatial distributions of emitted intensity, spectral shift, and linewidth) of Element 1 from the cross-sectional view. These fluorescence maps are obtained by analyzing the spatial variation of the spectral properties of the fluorescence line at around 940 nm, which belongs to the Nd³⁺ ion transition band of ${}^4F_{3/2} \rightarrow {}^4I_{9/2}$, which has been demonstrated to be a versatile fluorescence probe for the detection of slight structural modifications in the YAG network. In the femtosecond-laser induced filaments, an obvious modification of PL emission is observed, however, inside the central region (i.e., waveguiding core), the fluorescence features are well preserved with respect to the bulk. This confirms that the photonic structure Element 1 is an effective gain channel for the optical amplification and lasing. In addition, based on the μ PL maps, the refractive index change in the tracks (the contrast between individual modification and the unprocessed crystal) is determined to be $\Delta n \sim -4 \times 10^{-3}$, considering the combination of the damage induced refractive index reduction and the stress induced refractive index increment at the damage tracks and their surroundings²⁷. With the reconstructed spatial distribution of the refractive index, the modal profiles (Fig. 1g) of Element 1 along both TE and TM polarizations are calculated by Rsoft[®] software based on finite-difference beam propagation method (FD-BPM), showing reasonable agreement with the measured modal intensity distributions (Fig. 1d).

The light propagates in a straight way through Element 1. In order to implement beam manipulation, specially designed photonic elements are required to connect the basic one (i.e., Element 1) in a reasonable manner. Since the light propagates along the central core, one can introduce additional axial “defect” lines in appropriate positions to steer the beam propagation and tailor the intensity beam distribution. In addition, the area of the central-core region may be also changed to allow smooth and effective confinement of light beams. In this work, we present the 1×2 beam splitting and ring-shaped transformation, respectively, through two configurations of monolithic photonic structures.

Figures 2a and 2b show the schematic (left) and microscopic (right) of the Elements 2 and 3, which have been fabricated by introducing defect tracks in the core region of Element 1. The prototype with combination of Elements 1, 2 and 3, which are connected in sequence, is specially designed for 1×2 beam splitting (Fig. 2c). Figure 2d shows the beam profile evolution (simulated by FD-BPM) of 1064-nm light propagating along the three-element photonic structure. With Element 1, 2 and 3 connected in the sequence indicated by the scheme, a clear beam-profile splitting is observed at the waveguide output (Fig. 2e for experimental results) with measured intensity splitting ratio of 0.505 to 0.495 for the two arms, showing excellent performance for a Y-branch-like function.

Similarly, we perform the beam manipulation from a single-spot Gaussian profile to a ring-shaped one through connection of 3 elements. Figures 3a and 3b show the schematic (left) and optical image (right) corresponding to the Elements 4 and 5. The combination of Elements 1, 4, and 5 in a joint structure (see Fig. 3c for the prototype scheme) is designed for ring-shaped beam transformation. Figure 3d depicts the simulated beam profile evolution of light propagation through the structure at 1064 nm. It could be found that with the combination of Elements 1 and 4, a ring-shaped profile starts to be established; after additional connection of Element 5, the beam shape becomes a nearly perfect ring (Fig. 3e for experimental data). Please note these results are obtained experimentally in the “passive” operation regime, i.e., under input and output signals of a 1064-nm laser beam. In addition, it is worth pointing out that the output powers of

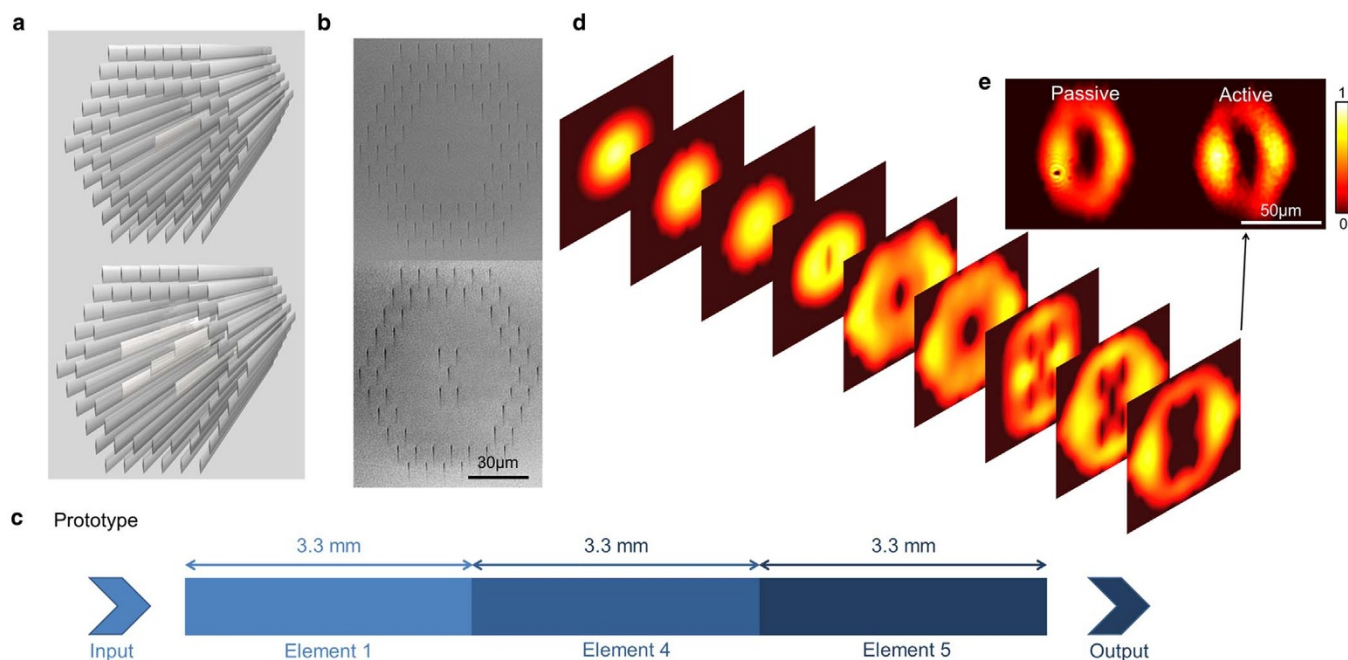


Figure 3 | Photonic structure characterization for ring-shaped transformation in passive regime. (a), Schematic images of Element 4 (top) and 5 (bottom). (b), Microscopic pictures of Element 4 (top) and 5 (below). (c), The prototype of the ring-shaped photonic structure with connection of Element 1, 4 and 5 with each element 3.3-mm long. (d), Simulated beam profile evolution as the 1064-nm light propagates along the ring-shaped photonic structure. (e), Measured intensity distributions of the ring-shaped structure in both passive and active regimes at 1064 nm.

the single-element waveguide and the three-element prototypes (i.e. 1 + 2 + 3 or 1 + 4 + 5) are nearly the same, showing that, in passive regime, the axial defects do not introduce additional losses, and the beam manipulation can be implemented in the photonic structures efficiently (see Supplementary Fig. 2).

In practice, for more compact geometry of photonic devices, the direct-pump lasing is on demand from waveguiding structures, i.e., the systems operate in the “active” regime. In straight channel waveguides, efficient lasers have been realized in many gain materials⁸; on the contrary, lasing structures capable of beam generation and manipulation were reported in limited literatures, such as curved waveguides in Yb:YAG crystals²³. In this work, we apply an optical direct-pump to the monolithic combination of the photonic elements to achieve manipulated guided lasers in CW regime. Figure 4a shows the schematic of the waveguide lasing experiment setup. The pump beam is taken at a wavelength of 808 nm from a Ti:Sapphire CW laser. The output lasing is at the wavelength of 1064 nm, which corresponds to the main emission line of the Nd³⁺ ion transition band ${}^4F_{3/2} \rightarrow {}^4I_{11/2}$. The obtained modal profiles at 1064 nm in the active regime are as same as those achieved in passive regime at same wavelength for corresponding combinations of photonic elements. The measured CW laser spectrum is depicted in Fig. 4b, centering at 1064 nm. Figure 4c shows the output laser powers at 1064 nm as a function of launched pump power for the three-element beam splitting and ring-shape-transformation structures, respectively. For comparison, the lasing performance curve for a single Element 1 structure is also depicted in this figure. As the launched pump power is above a threshold (180 mW), lasing oscillations are observed in the photonic structure systems. For the beam-splitting structure (Element 1 + 2 + 3), the laser shows a slope efficiency of 32% and a maximum output power of 241 mW. For the ring-shaped structure (Element 1 + 4 + 5), the laser operates with a slope efficiency of 29%, climbing to a maximum output power of 224 mW in case of a pump power of 0.95 W. Compared with the lasing performance based on a single Element 1 (with slope efficiency of 45% and maximum output power of 350 mW), i.e., a straight photonic structure, there are 30% and 35% loss of maximum output

power for the beam splitted and ring-shaped configurations, respectively. This should be mainly attributed to the additional losses from the splitted lasing cavity, i.e., non-perfect Fabry-Perot cavity, as the losses from the introduction of axial defects are negligible in passive regime. These loss values in active regime are comparable to those of the curved Yb:YAG waveguide lasers (with a loss of $\sim 20\%$ with respect to the straight waveguide lasers)²³. Nevertheless, such losses could be further reduced by optimizing the parameters of the femtosecond-laser writing and dimensions of each element. In addition, the lasing performance could be also improved by an optimized pump system, reaching higher slope efficiency and Watt-level maximum output powers.

Pulsed lasers are required in high-intensity applications, such as nonlinear optics. Graphene is a low-cost 2D nano-scale material, which has been widely applied in many fields^{28,29}. It has been proved to be an ideal material for fabrication of ultra-broadband saturable absorbers (SAs) owing to the linear energy dispersion relation and fast responses^{30,31}. In this work, a graphene SA mirror is attached on the crystal end face to obtain passive Q-switched lasers from the photonic structures. The measured Q-switched laser spectrum and the pulse train are depicted in Fig. 4b. The central wavelength of 1064 nm is consistent with the case of CW operation. The inset in Fig. 4b shows the pulse train of the Q-switched waveguide laser. Figure 4d illustrates the average output powers of the single Element 1, 3-element beam splitting, and ring-shape-transformation structures, as functions of launched pump power at 808 nm, respectively. From the linear fit of the experimental data, we have determined that the lasing thresholds for pulsed lasers are all around 265 mW, which is slightly higher than those of CW regimes. Above the lasing threshold, the Q-switching operates pulsed lasers with slope efficiencies of 35%, 24%, and 22% and maximum output powers of 243, 163, and 148 mW for these three configurations, respectively. In addition, by varying the pumping power, the repetition rates of pulsed lasers from the single Element 1, 3-element beam splitting, and ring-shape-transformation structures could be tuned from less than 1 MHz to above 4 MHz (as depicted in Fig. 4e), when the pumping power is increased from 265 mW to 950 mW.

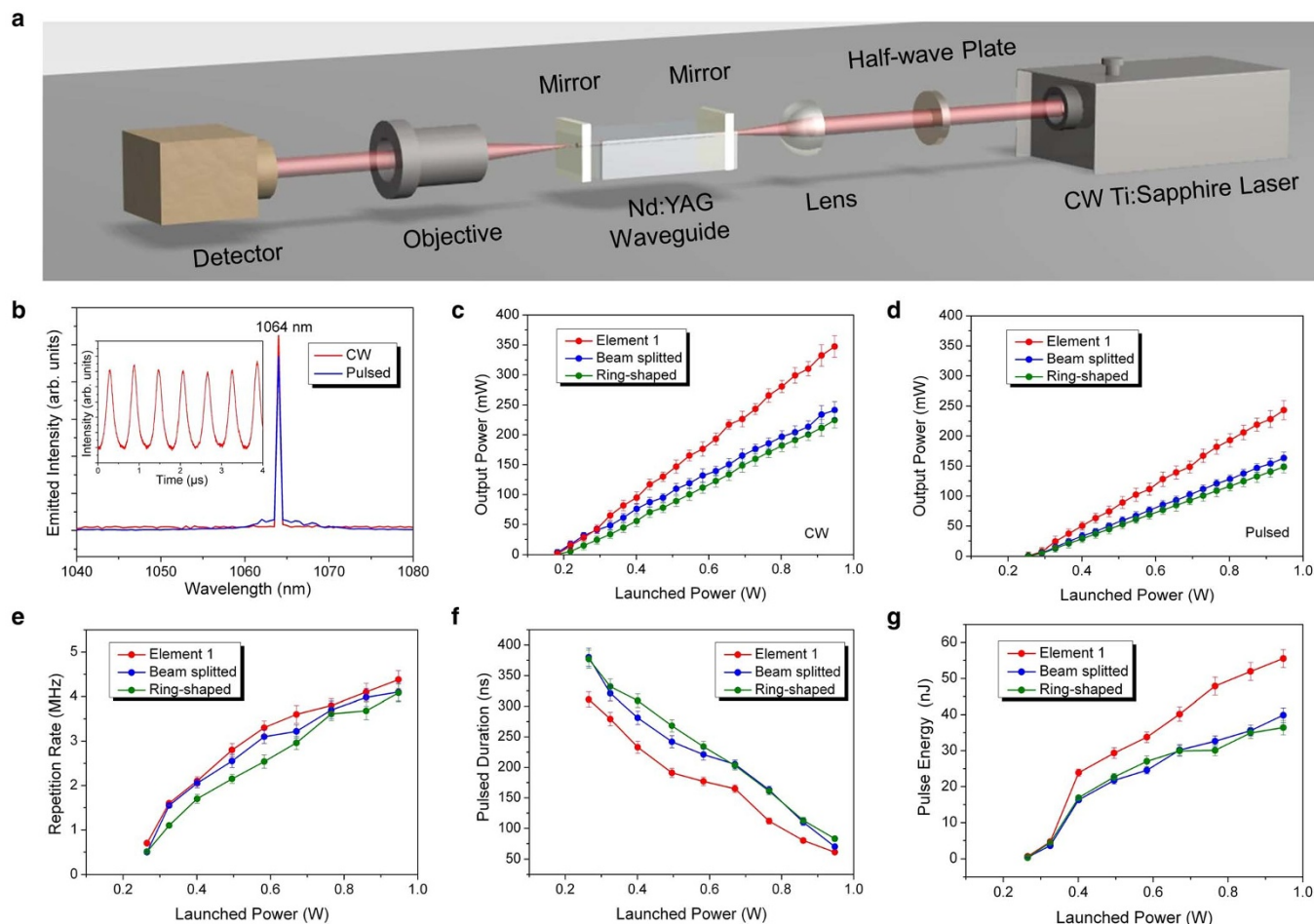


Figure 4 | Lasing with beam manipulation. (a), Schematic of experimental arrangement for the laser generation in Nd:YAG photonic structure in both CW and pulsed regimes. (b), Laser emission spectrum from the Nd:YAG waveguide in CW and graphene-SA Q-switched regimes. The inset shows the pulse train of the Q-switched waveguide laser. (c), Output laser powers from Element 1, beam splitter and ring-shaped structures as functions of the launched pump in CW regime. (d), Output laser powers from Element 1, beam splitter and ring-shaped structures as functions of the launched pump in pulsed regime. (e), Repetition rate of the Q-switched pulsed lasers. (f), Q-switched pulse durations as functions of launched pump power. (g), Q-switched single-pulse energies as functions of launched pump power.

Meanwhile, the pulse duration varies from 300 ns to around 70 ns (Fig. 4f). Finally, the maximum single pulse energy is ~ 40 nJ for the 3-element beam splitting and ring-shape-transformation structures, which is lower than that (~ 55 nJ) for the single Element 1 (Fig. 4g).

Discussion

We have designed and fabricated in a Nd:YAG laser crystal wafer a novel family of monolithic photonic structures consisting of hexagonal lattices of laser-damage bits with induced axial defects that act as guiding cores. The integration of a few specially designed photonic elements with defect lines has been demonstrated to be an efficient and simple way to build compact structures capable of efficient beam profile manipulation, including basic functions of beam splitting and ring-shaped transformation. Efficient lasing in both CW and pulsed regimes are implemented, demonstrating that the monolithic photonic structures are capable of not only light manipulation but also efficient light generation. Our work paves a solid way for a wide variety of applications in many disciplines. On one side, from the fabrication point of view, our work shows the capability of femtosecond laser microfabrication to produce more complex waveguiding devices by integration of more designable elements in a single crystal chip, which would further enlarge the scope of promising applications related to this fabrication technique. In addition, unlike laser glasses in which femtosecond laser writing is easily used to

produce 3D waveguiding structures, in crystalline laser materials it is considerably difficult since the femtosecond laser irradiation typically produces negative index decreases in the tracks. Our work suggests a solution to realize lasing with 3D beam manipulation in crystalline platforms. As a simple example, our simulation has shown that, by using 3-Element integration, a $3D 1 \times 4$ beam splitter can be fabricated under the similar approach (see Supplementary Fig. 3). Therefore, one could expect highly compressed laser devices for light guiding and beam manipulation, to satisfy some special requirements for particular applications. On the other side, this technique could be extended to other doped YAG crystals for ultra-broadband applications. For example, if the platforms of Tm:YAG or Er:YAG are used^{32,33}, the generated laser wavelength could be extended to mid-infrared. In case of Yb:YAG chips³⁴, the mode-locking of the waveguide laser enables the generation of ultrashort pulses of femtosecond temporal durations. These new miniature laser sources with different wavelength or operation regimes could be utilized in broader-scope applications of both scientific researches and human life. Finally, one could exploit the application of this technique to other crystals to obtain waveguide devices, such as frequency converters (second harmonic generation), frequency comb generators, integrated elements for biophotonics, etc. In conclusion, this work demonstrates a novel family of monolithic photonic structures and their performance as beam shapers or as laser sources with controlled



output properties. Strong capability of fabrication of various photonic devices by this simple and flexible technique is also shown in a designable manner for circuit production.

Methods

Fabrication of photonic structures. To fabricate the photonic structures in the Nd:YAG crystal we use the ultrafast-laser direct inscription with the sample-scanning approach. The Nd:YAG (doped by 1 at.% Nd³⁺ ions) crystal wafer is cut with dimension of $9.9 \times 10 \times 2 \text{ mm}^3$ and optically polished. An amplified Ti:Sapphire femtosecond laser (Spitfire, Spectra Physics) that delivered linearly-polarized pulses with a temporal duration of 120 fs, a central wavelength of 795 nm and operating at a repetition rate of 1 kHz, is used as the laser source. The beam is focused by a $20\times$ microscope objective and the average power is reduced to 1.2 mW (measured after the objective) by using a set of half-wave plate and linear polarizing cube, and a calibrated neutral density filter. The laser irradiation is controlled with a mechanical shutter. The sample is placed on a XYZ micro-positioning stage that allowed scanning the sample at constant velocity ($500 \mu\text{m/s}$) while irradiating from the surface of $9.9 \times 10 \text{ mm}^2$ with the femtosecond pulses at certain depth beneath the surface ($\sim 150 \mu\text{m}$): under our experimental conditions, a damage track is then produced with a transverse length of $\sim 10 \mu\text{m}$. A number of parallel scans of the sample are done at different heights in order to obtain the desired hexagonal photonic structures.

Characterization of guidance and fluorescence. The waveguiding performance is carried out under a typical end-face arrangement. A linearly polarized CW solid state laser with single wavelength of 1064-nm is utilized as the light source. The polarized light beam is focused by a $20\times$ microscope object lens, and the coupling into the photonic structures. Another microscope object lens is used as the out-coupler, through which the transmitted light is collected and imaged by a CCD camera. The light powers are measured by a few powermeters. The propagation losses of the photonic structures are determined by directly measurement of the light powers from the input and output end-faces.

The μ -PL spectra are excited by a 488-nm CW diode laser. The light beam is focused in the sample by a $50\times$ microscope objective (N.A. ~ 0.55), thus yielding a spot with a diameter of approximately $0.53 \mu\text{m}$. The subsequent emission of Nd³⁺ ions is collected by the same microscope objective and, after passing through filters, lenses and pinholes, is analyzed by a high-resolution spectrometer. The software LabSpec® and WSxM® are used to analyze and fit the spectra and process the fluorescence images in terms of the spectral intensity, energy shift, and width of the fluorescence lines³⁵.

Refractive index reconstruction. The refractive index changes of the structures are obtained by the procedure described in Ref. 27. Briefly, the refractive index map is constituted by the superposition of the damage induced refractive index modification (reduction) and the stress field induced refractive index map (refractive index increment at compressed volumes). The first is obtained from the fluorescence images based on the fluorescence intensity as the fluorescence intensity reduction in respect to the bulk material is, in a first order approximation, assumed proportional to the laser-induced damage in the Nd:YAG network. The conversion of laser induced-damage into refractive index reduction is performed by a reference Nd:YAG sample that contains different damage tracks fabricated under the same conditions of femtosecond laser irradiation. The stress-induced refractive index map has been calculated from the fluorescence map obtained in terms of the induced spectral shift of Nd³⁺ fluorescence lines. From the spectral shift, one calculate the spatial variation of residual stress and from this the relative change in the unit cell volume (i.e. the lattice dilatation/densification). Finally, the refractive index modification is calculated by applying the Claussius-Mossotti approximation²⁷.

Lasing generation. The laser operation experiments in CW and pulsed regimes are both performed by utilizing an end pumping system. A polarized light beam at a wavelength of 808 nm is generated from a tunable CW Ti:Sapphire laser (Coherent MBR-100). A convex lens with focus length of 25 mm is used to couple the laser beam into the photonic structures; the radius of the incident pump laser beam is approximately 0.75 mm at $1/e^2$ position. For the CW waveguide laser systems, an input mirror (with the transmission of 98% at 808 nm and the reflectivity $>99\%$ at $\sim 1064 \text{ nm}$) and an output mirror (with the reflectivity $>99\%$ at 808 nm and 60% at $\sim 1064 \text{ nm}$, respectively), are adhered to the input and output end face of the waveguide respectively, constructing the Fabry-Perot lasing resonant cavity. Here, a set of mechanical bindings are employed to make the SA closely attached to the output facet of the waveguide sample. For the Q-switched pulsed laser generation, the output mirror is replaced by a bilayer graphene thin film coated on a fused silica glass plate as the SA. The graphene film is grown by chemical vapor deposition (CVD) on copper and nickel firstly, and then transferred to a fused silica glass. The transmission of the graphene film coated output mirror is measured to be $\sim 70\%$ at 1064 nm. The generated lasers are collected by utilizing a $20\times$ microscope objective lens (numerical aperture N.A. = 0.4) and imaged by using an infrared CCD. We use a spectrometer with resolution of 0.2 nm to analyze the emission spectra of the laser beams. The schematic plot of the experimental setup for the CW and pulsed laser oscillations are depicted in Fig. 4a.

- Sohler, W. *et al.* Integrated optical devices in lithium niobate. *Opt. Photon. News* **19**, 24–31 (2008).
- Matthews, J. C. F., Politi, A., Stefanov, A. & O'Brien, J. L. Manipulation of multiphoton entanglement in waveguide quantum circuits. *Nature Photon.* **3**, 346–350 (2009).
- Crespi, A. *et al.* Integrated photonic quantum gates for polarization qubits. *Nat. Commun.* **2**, 566 (2011).
- Schmidt, H. & Hawkins, A. R. The photonic integration of non-solid media using optofluidics. *Nature Photon.* **5**, 598–604 (2011).
- Saglamiyurek, E. *et al.* Broadband waveguide quantum memory for entangled photons. *Nature* **469**, 512–515 (2011).
- Yang, Y. *et al.* Optofluidic waveguide as a transformation optics device for lightwave bending and manipulation. *Nat. Commun.* **3**, 651 (2012).
- Albrecht, B., Farrera, P., Fernandez-Gonzalvo, X., Cristiani, M. & de Riedmatten, H. A waveguide frequency converter connecting rubidium-based quantum memories to the telecom C-band. *Nat. Commun.* **5**, 3376 (2014).
- Grivas, C. Optically pumped planar waveguide lasers, Part I: Fundamentals and fabrication techniques. *Prog. Quant. Electron.* **35**, 159–239 (2011).
- Calmano, T. *et al.* Crystalline Pr:SrAl₁₂O₁₉ waveguide laser in the visible spectral region. *Opt. Lett.* **36**, 4620–4622 (2011).
- Grivas, C., Corbari, C., Brambilla, G., Pavlos, G. & Lagoudakis, P. G. Tunable, continuous-wave Ti:sapphire channel waveguide lasers written by femtosecond and picosecond laser pulses. *Opt. Lett.* **37**, 4630–4632 (2012).
- Tan, Y. *et al.* 70% slope efficiency from an ultrafast laser-written Nd:GdVO₄ channel waveguide laser. *Opt. Express* **18**, 24994–24999 (2010).
- Mary, R. *et al.* 1.5 GHz picosecond pulse generation from a monolithic waveguide laser with a graphene-film saturable output coupler. *Opt. Express* **21**, 7943–7950 (2013).
- Macdonald, J. R. *et al.* Efficient mid-infrared Cr:ZnSe channel waveguide laser operating at 2486 nm. *Opt. Lett.* **38**, 2194–2196 (2013).
- Gattass, R. R. & Mazur, E. Femtosecond laser micromachining in transparent materials. *Nature Photon.* **2**, 219–225 (2008).
- Sugioka, K. & Cheng, Y. Ultrafast lasers—reliable tools for advanced materials processing. *Light Sci. Appl.* **3**, e149 (2014).
- Ams, M., Marshall, G. D., Dekker, P., Piper, J. A. & Withford, M. J. Ultrafast laser written active devices. *Laser & Photon. Rev.* **3**, 535–544 (2009).
- Davis, K. M., Miura, K., Sugimoto, N. & Hirao, K. Writing waveguides in glass with a femtosecond laser. *Opt. Lett.* **21**, 1729–1731 (1996).
- Osellame, R., Hoekstra, H. J., Cerullo, G. & Pollnau, M. Femtosecond laser microstructuring: an enabling tool for optofluidic lab-on-chips. *Laser & Photon. Rev.* **5**, 442–463 (2011).
- Chen, F. & Vazquez de Aldana, J. R. Optical waveguides in crystalline dielectric materials produced by femtosecond-laser micromachining. *Laser & Photon. Rev.* **8**, 251–275 (2014).
- Crespi, A. *et al.* Anderson localization of entangled photons in an integrated quantum walk. *Nature Photon.* **7**, 322–328 (2013).
- Tillmann, M. *et al.* Experimental boson sampling. *Nature Photon.* **7**, 540–544 (2013).
- Rechtsman, M. C. *et al.* Photonic Floquet topological insulators. *Nature* **496**, 196–200 (2013).
- Calmano, T., Paschke, A. G., Müller, S., Kränkel, C. & Huber, G. Curved Yb:YAG waveguide lasers, fabricated by femtosecond laser inscription. *Opt. Express* **21**, 25501–25508 (2013).
- Liu, H., Jia, Y., Vazquez de Aldana, J. R., Jaque, D. & Chen, F. Femtosecond laser inscribed cladding waveguides in Nd:YAG ceramics: Fabrication, fluorescence imaging and laser performance. *Opt. Express* **20**, 18620–18629 (2012).
- Calmano, T., Siebenmorgen, J., Hellmig, O., Petermann, K. & Huber, G. Nd:YAG waveguide laser with 1.3 W output power fabricated by direct femtosecond laser writing. *Appl. Phys. B* **100**, 131–135 (2010).
- Okhrimchuk, A., Mezentssev, V., Shestakov, A. & Bennion, I. Low loss depressed cladding waveguide inscribed in YAG:Nd single crystal by femtosecond laser pulses. *Opt. Express* **20**, 3832–3843 (2012).
- Ródenas, A. *et al.* Refractive index change mechanisms in femtosecond laser written ceramic Nd:YAG waveguides: micro-spectroscopy experiments and beam propagation calculations. *Appl. Phys. B* **95**, 85–96 (2009).
- Novoselov, K. S. *et al.* Two-dimensional gas of massless Dirac fermions in graphene. *Nature* **438**, 197–200 (2005).
- Bao, Q. *et al.* Broadband graphene polarizer. *Nature Photon.* **5**, 411–415 (2011).
- Bonaccorso, F., Sun, Z., Hasan, T. & Ferrari, A. C. Graphene photonics and optoelectronics. *Nature Photon.* **4**, 611–622 (2010).
- Martinez, A. & Sun, Z. Nanotube and graphene saturable absorbers for fibre lasers. *Nature Photon.* **7**, 842–845 (2013).
- Gao, C., Gao, M. & Zhang, Y. Stable single-frequency output at 2.01 μm from a diode-pumped monolithic double diffusion-bonded Tm:YAG nonplanar ring oscillator at room temperature. *Opt. Lett.* **34**, 3029–3031 (2009).
- Ziolk, C. *et al.* High-repetition-rate, high-average-power, diode-pumped 2.94- μm Er:YAG laser. *Opt. Lett.* **26**, 599–601 (2001).
- Prinon, O. *et al.* High-power 200 fs Kerr-lens mode-locked Yb:YAG thin-disk oscillator. *Opt. Lett.* **36**, 4746–4748 (2011).



35. Horcas, I. I. *et al.* WSXM: A software for scanning probe microscopy and a tool for nanotechnology. *Rev. Sci. Instrum.* **78**, 013705 (2007).

Acknowledgments

This work was supported by National Natural Science Foundation of China (No. 11274203), Specialized Research Fund for the Doctoral Program of Higher Education of China (No. 20130131130001), and Junta de Castilla León under project SA086A12-2.

Author contributions

Y.J., C.C., Y.T. and F.C. performed all the experiments and simulation of guidance, beam propagation and manipulation, and lasing of the photonic microstructures. J.R.V.A. and F.C. conceived and designed the photonic microstructures. J.R.V.A. and G.R.C. implemented the fabrication of photonic structures. B.R.R. and D.J. performed μ PL measurements of the structures. All the authors discussed the results and participated in the manuscript preparation.

Additional information

Supplementary information accompanies this paper at <http://www.nature.com/scientificreports>

Competing financial interests: The authors declare no competing financial interests.

How to cite this article: Jia, Y. *et al.* Monolithic crystalline cladding microstructures for efficient light guiding and beam manipulation in passive and active regimes. *Sci. Rep.* **4**, 5988; DOI:10.1038/srep05988 (2014).



This work is licensed under a Creative Commons Attribution-NonCommercial-NoDerivs 4.0 International License. The images or other third party material in this article are included in the article's Creative Commons license, unless indicated otherwise in the credit line; if the material is not included under the Creative Commons license, users will need to obtain permission from the license holder in order to reproduce the material. To view a copy of this license, visit <http://creativecommons.org/licenses/by-nc-nd/4.0/>